

PAPER

Angle-resolved light scattering of single human chromosomes: experiments and simulations

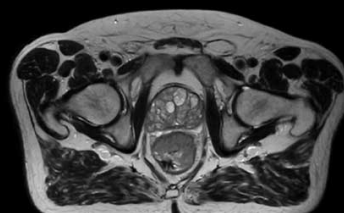
To cite this article: Dennis Müller *et al* 2019 *Phys. Med. Biol.* **64** 045016

View the [article online](#) for updates and enhancements.

Uncompromised.

See clearly during treatment to attack
the tumor and protect the patient.

Two worlds, one future.



Captured on Elekta high-field MR-linac during 2018 imaging studies.

 **Elekta**

Elekta MR-linac is pending 510(k) premarket
clearance and not available for commercial
distribution or sale in the U.S.



PAPER

Angle-resolved light scattering of single human chromosomes: experiments and simulations

RECEIVED
2 October 2018REVISED
19 December 2018ACCEPTED FOR PUBLICATION
10 January 2019PUBLISHED
18 February 2019Dennis Müller^{1,3}, Daniel Geiger², Julian Stark¹ and Alwin Kienle¹¹ Institute for Lasertechnologies in Medicine and Metrology (ILM), Helmholtzstr. 12, 89081 Ulm, Germany² Institute for Experimental Physics, Ulm University, Albert-Einstein-Allee 11, 89081 Ulm, Germany³ Author to whom any correspondence should be addressed.E-mail: dennis.mueller@ilm-ulm.de**Keywords:** light scattering, angle resolved, chromosome, scatterer geometry, scatterer orientation, discrete dipole approximation, atomic force microscopy**Abstract**

Angle-resolved light scattering measurements of human metaphase chromosomes were compared to the results of numerical light scattering simulations with geometrical models based on atomic force microscopy (AFM) measurements of the same chromosomes. The simulations were conducted using the discrete dipole approximation method (DDA), which solves Maxwell's equations for induced dipoles, positioned in a discrete lattice. A remarkable agreement between the light scattering simulations and measurements of all 6 studied chromosomes was found. Additionally, the influence of small changes in the orientation of a complex scatterer geometry on its angle-resolved scattering pattern is shown. A method is presented to approximate such variations in the scatterer's orientation by a linear shift of the angular scattering pattern. This method provides an initial guess on the scatterer's orientation, reducing the amount of simulations needed considerably. It was validated on simulations of a cuboid and successfully applied in the evaluation of the chromosome measurements.

1. Introduction

Light scattering is of interest in many fields of research, from nanoparticles (Lukyanchuk *et al* 2015, Lee *et al* 2017) to extrasolar giant planets (Seager *et al* 2000, Sudarsky *et al* 2000). The scattered light yields information about the scatterer's size (Mullaney *et al* 1969, Chylek *et al* 1983, Goddeeris *et al* 2006, Schmitz *et al* 2011, Rothe *et al* 2012, Fischer and Schmidt 2016), shape (Santos and Castanho 1996, Pencer *et al* 2001, Konokhova *et al* 2013), inner structure (Stark *et al* 2016) and material properties, such as the refractive index (RI) (Chylek *et al* 1983). Additionally, light scattering methods are generally non-invasive, fast, and can be applied to isolated scatterers (Jo *et al* 2014, 2015), suspensions (Goddeeris *et al* 2006), aerosols (Lane *et al* 2018, Lew *et al* 2018) or even impurities in solid samples (Peelen and Metselaar 1974, Otero *et al* 2010). Due to these characteristics, light scattering has been applied to numerous biological samples, such as spores (Bickel and Stafford 1981), bacteria (Bickel and Stafford 1981, Diaspro *et al* 1995, Konokhova *et al* 2013, Jo *et al* 2014, 2015), blood cells (Bickel and Stafford 1981), cell morphology (Perelman *et al* 1998, Wax *et al* 2002, Drezek *et al* 2003, Stark *et al* 2016) and chromosomes (Rebner *et al* 2016). Angle-resolved light scattering can be measured directly (Maltsev 2000, Schmitz *et al* 2011, Rothe *et al* 2012, Stark *et al* 2016) or indirectly via Fourier transform light scattering (FTLS) (Ding *et al* 2008, Jo *et al* 2014, 2015), where the angular scattering pattern is calculated from measured spatial and phase information.

The geometrical structure of human chromosomes has been studied before with various methods, such as scanning electron microscopy (SEM) (Harrison *et al* 1985, Wanner *et al* 2005), or atomic force microscopy (AFM) (Tamayo 2003a, 2003b, Ushiki and Hoshi 2008). These studies give insight on the geometrical macro- and microstructure of human chromosomes. The discrimination of chromosomes, on the other hand, is usually done with the use of marker substances. Common methods are giemsa banding (Drets and Shaw 1971, Patil *et al* 1971) and fluorescence *in situ* hybridisation (FISH) (Caspersson *et al* 1970, Levsky and Singer 2003). Both techniques rely on labelling certain areas of the chromosome and identifying it through the resulting pattern.

The method applied in this work uses the correlation between light scattering measurements and light scattering simulations to obtain information about geometrical parameters of the chromosomes. In general, this is done by varying the geometry of the scatterer in light scattering simulations, creating a set of scattering patterns. The measurement results are correlated with said set. From the highest correlation between simulation and measurement, the geometrical parameters of the complex scatterer are identified. This method has been validated on spherical scatterers before (Schmitz *et al* 2011, Rothe *et al* 2012). In the present study, chromosomes are measured angle-resolved with a light scattering microscope and subsequently with an atomic force microscope. From the latter measurement, models for numerical light scattering simulations are created and compared to the measurements. Variation parameters were the chromosomes' orientation and shape.

2. Materials and methods

2.1. Sample preparation

The following description of air dried metaphase chromosome preparation from human peripheral blood is based on the works of Moorhead *et al* (1960) with alterations due to manufacturer information and our technical assistant's experiences.

0.7 ml of heparinized, peripheral blood from a healthy, male, human donor was mixed with 8 ml chromosome medium b (containing phytohemagglutinin (PHA)L) and incubated for 48 h at 37 °C and 5 % CO₂ in a sterile environment. The cultivation process was stopped by the addition of 100 µl of colcemid solution (10 µg ml⁻¹), followed by a second incubation for 40 min at 37 °C. Subsequently, the culture was centrifuged for 10 min at 950 rpm. The supernatant was withdrawn by suction and the pellet resuspended in the residual. The hypotone shock was induced by the addition of 1 ml of 0.075 M KCl solution, resuspension, followed by another addition of 5 ml KCl solution, resuspension and an incubation for 15 min in a 37 °C waterbath. Then, the culture was centrifuged for 10 min at 950 rpm, the supernatant removed and the pellet resuspended in the leftover fluid. Fixation was achieved, by stepwise addition of methanol:acetic acid (3:1) and resuspension. In the first step 1 ml was added, in the subsequent two steps 4 ml. Thereafter, the culture was incubated for 30 min at 4 °C, and centrifuged again, as described previously. After fixation, the washing was performed by a fourfold addition of 5 ml of the fixative, resuspension, and centrifugation for 10 min at 950 rpm.

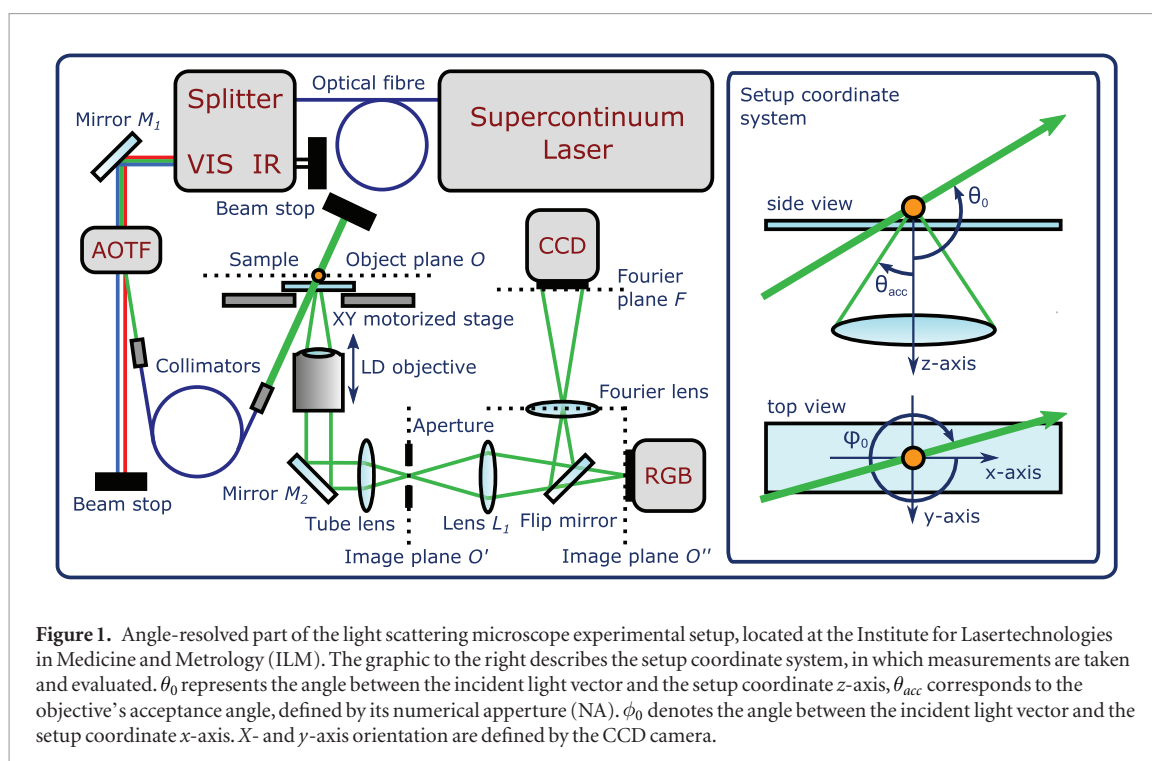
Cover glasses of the dimensions 1 cm by 1 cm were stored in methanol for one day and then rinsed for 10 min with water. Afterwards, the cover glasses were cleaned with double-distilled water and stored at 4 °C. After another centrifugation and resuspension, 5–10 drops of the incubated cell suspension were dropped from a height of about 20 cm onto the cover glasses and air dried. The presence of mitoses on the cover glass was checked with a phase contrast microscope.

2.2. Scattering light microscope

The experimental setup of the light scattering microscope with its two detection paths, spectrally resolved and angularly resolved, has been described thoroughly elsewhere (Stark *et al* 2016). This setup has been validated on polystyrene microspheres, demonstrating a sensitivity to geometrical changes of single scatterers in the range of nanometres (Schmitz *et al* 2011, Rothe *et al* 2012). The present work makes use of the angle-resolved detection path, therefore only a short introduction to this part of the setup is presented.

The light scattering microscope setup consists of an inverse microscope (Axiovert 135, Carl Zeiss AG, Oberkochen, Germany), used in darkfield illumination mode. A supercontinuum laser (SuperK Blue, NKT Photonics A/S, Birkerød, Denmark) combined with an acousto-optical tuneable filter (AOTF) (AOTF-PCAOM Vis, Crystal Technology, LLC, Palo Alto, California) acts as the light source, providing quasi-monochromatic light with a continuously tuneable wavelength between 420 nm and 700 nm. The linear polarisation of the AOTF output is lost during the transmission through a single mode fibre (FD7 FC/PC, NKT Photonics A/S, Birkerød, Denmark), which is mounted with collimators on both ends. The fibre directs the illumination light, which is 1 mm in diameter after leaving the fibre, towards the sample with an incident polar angle θ_0 of 121° and an azimuthal angle ϕ_0 of 341°, as defined in figure 1. The z-axis of the setup coordinate system is located on the optical axis of the objective, pointing towards the detection path. The x- and y-axes are defined to be aligned with the orientation of the CCD camera chip. The setup coordinate system and the incident light angles are depicted in figure 1 for clarity.

The inverted microscope is outfitted with a long distance objective (LD EC Epiplan-Neofluar 50x/0.55 HD DIC M27 air, Carl Zeiss AG, Oberkochen, Germany) with an effective numerical aperture (NA_{eff}) of 0.53, which translates to an acceptance angle θ_{acc} of 32° for samples surrounded by air. Thus scattering angles from 89° to 153° can be detected. The angle-resolved scattering pattern is recorded by a CCD camera (SIS p1010, Theta Systems GmbH, Gröbenzell, Germany), located in the Fourier plane. The illuminated area on the CCD chip, which represents an angular range of 64° is 335 pixels in diameter, resulting in an angular resolution between 0.15°/pixel for larger polar angles θ and about 0.22°/pixel for the centre, due to the sinusoidal nature of the angle distribu-



tion, when projected on a plane. Inside the detection path, in the image plane, a pinhole is located, which is used to adjust the CCD camera's field of view. Its size, varying from $200\ \mu\text{m}$ to $600\ \mu\text{m}$, can be adjusted to ensure that only the selected scatterer contributes to the recorded signal. The pinhole sizes correspond to diameters between $4\ \mu\text{m}$ and $12\ \mu\text{m}$ in the object plane.

2.3. Measurements

2.3.1. Light scattering measurements

Angle-resolved light scattering measurements were performed on single human chromosomes in metaphase. Inside each set of chromosomes, the ones separable by the circular pinholes were used for measurements. The cover glass was rotated to position the chromosomes with their long axis orthogonal to the incident light beam. The long axis was defined by a line, connecting the middle of the ends of the q-arms and the middle of the ends of the p-arms, as shown in figure 2. The sample was illuminated with non-polarised, quasi-monochromatic light with a wavelength of $543 \pm 3\ \text{nm}$ and the angular scattering pattern was recorded. The smallest pinhole, still fitting the chromosome, was used to cut off the high angular frequency signals from organic debris in the surrounding area. Such debris could otherwise distort the chromosomes scattering pattern in a speckle-like manner.

Each recorded image of the scattering pattern was cut at the border of the circular observable solid angle, the background was subtracted and the intensity normalized to its maximum. Furthermore the measurements were interpolated onto a lattice with 400 by 400 points, for easy correlation with the simulation data. The interpolation was conducted linearly with Matlab's `TriScatterInterp()` function (MATLAB, R2011b, MathWorks).

2.3.2. Atomic force microscope measurements

AFM measurements were carried out on a MultiMode SPM (Bruker MMAFM-2, Bruker Corporation, USA) with silicon cantilevers (OMCL-AC240TS-R3, Olympus Corporation, Japan). The used cantilever type had a low spring constant of $2\ \text{N m}^{-1}$, a small typical tip radius of $7\ \text{nm}$ and a tip half angle of less than 17.5° . Therefore it is a reasonable choice for imaging of relatively soft objects with challenging aspect ratios like chromosomes. Measurements were done in tapping mode in order to reduce shear forces to the sample during scanning. Post processing of the measurements was carried out using Gwyddion (Neas and Klapetek 2012). Measurement artefacts like bow and tilt were corrected by subtraction of a polynomial fit to the background that was the flat substrate. Operations were carried out using only background pixels that were selected by a height threshold mask.

2.4. Simulations

The actual light scattering measurements are the first step to determine the optical and geometrical properties of the scatterer. Without correlation to suitable simulation data, only elementary assertions about symmetry, size and general shape can be made. First, a suitable simulation method has to be chosen.

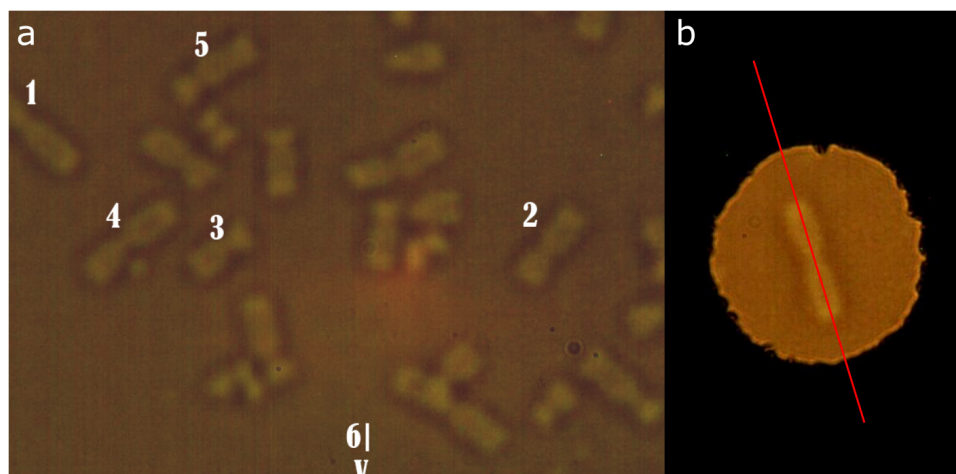


Figure 2. Images of chromosomes used for the data of this work. (a) Shows the set of chromosomes with their orientations and sequence numbers. (b) Depicts chromosome 1 prior to the presented measurements. The $600\ \mu\text{m}$ pinhole was used, which corresponds to a diameter of $12\ \mu\text{m}$ in the object plane. The long axis, which was manually oriented perpendicular to the incident light, is marked red.

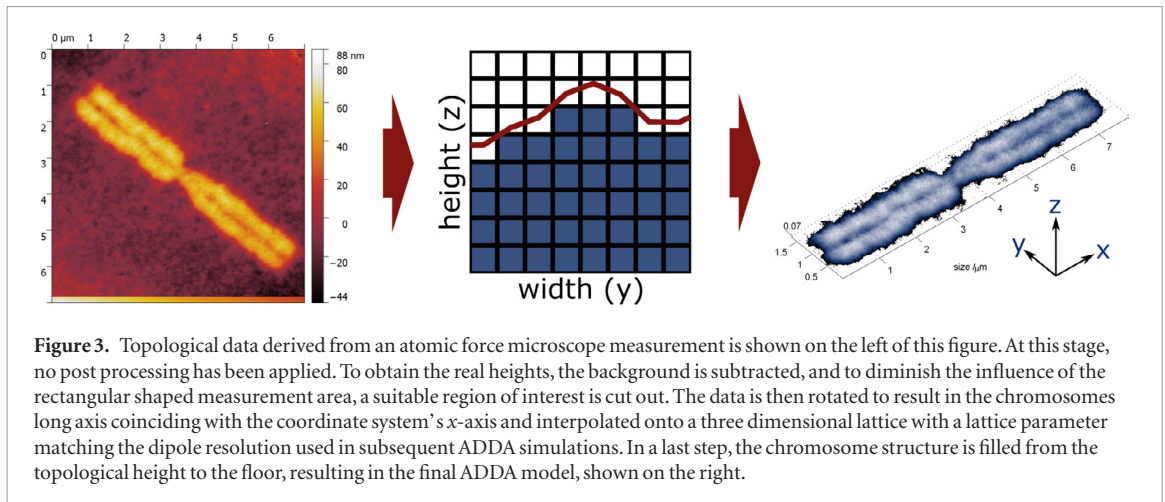
Analytical solutions for light scattering on particles are only available for special geometries, like spheres (Mie 1908), cylinders, spheroids, and multiple spheres and cylinders, including concentric arrangements of spheres and cylinders, respectively. The T -matrix method (Waterman 1965) represents a generalization of Mie's method and allows the handling of slightly more complex scatterers. All other geometries have to be studied with numerical simulations. One common approach is the Discrete Dipole Approximation method (DDA). The scatterer is modelled through a lattice of polarisable points, which under the effect of an incident electromagnetic wave gain a dipole moment. Maxwell's equations are solved for this set of discrete dipoles (Purcell and Pennypacker 1973, Draine and Flatau 1994). Several implementations of this method are available, such as DDSCAT (Draine and Flatau 2008), OpenDDA (Donald *et al* 2009) and Amsterdam Discrete Dipole Approximation (ADDA) (Yurkin and Hoekstra 2011). Another common approach is the Finite Difference Time Domain method (FDTD), which simulates the passing of a light pulse through a lattice of different refractive indices in finite time steps. When assuming no dispersion, multiple wavelengths can be computed with little additional effort.

The performances of the DDA and the FDTD method have been compared systematically before (Yurkin *et al* 2007). It was found that the DDA method is by an order of magnitude faster than FDTD, when studying large scatterers with a relative refractive index ≤ 1.2 , while large scatterers with a relative RI of ≥ 1.7 are simulated faster by the same amount with FDTD. A relative RI of 1.4 was named to be the border, where both methods perform equally. The relative refractive index describes the ratio between the refractive index of the scatterer and the refractive index of its surrounding medium. The chromosome's surrounding medium was air with a RI of 1.0 in the present work, hence the relative RI equals the absolute RI here. The refractive index of DNA has been determined in a study of Kwon *et al* (2012), and was found to be 1.53–1.54 in bulk material for wavelengths between 500 nm and 600 nm. In other works (Shemilt *et al* 2015), chromosomes were assumed to consist of solid DNA, with a RI of 1.54. In contrast to that, a porous structure with an effective refractive index of 1.4 was used in the present work. Similar assumptions, concerning the RI value of chromosomes, have been made by Khatibzadeh *et al* (2014). They used an RI for chromosomes in the region from 1.36 to 1.40. With an effective RI of 1.4, either option of the numerical simulation methods was suitable. All light scattering simulations in the present work were performed with the open source implementation Amsterdam discrete dipole approximation (ADDA).

The models used by the ADDA code are three dimensional, equidistant lattices, where each cell holds a refractive index (RI). In this lattice, the near field of the scattering is solved and subsequently for each scattering angle a near to far field transformation performed that yields a Mueller Matrix for each angle pair (θ_s, ϕ_s) . The Mueller matrices, obtained by ADDA simulations, are used in the Stokes formalism (Stokes *et al* 1852).

2.4.1. Model generation

The models used in the following ADDA simulations were constructed from the topological data obtained through AFM measurements. This data has already been background subtracted and laterally cut out to a region of interest. Furthermore, it was rotated in the sample plane, to align the chromosomes long axis in x -direction to prepare the chromosome orientation for the simulations according to the experiment. The topological data was interpolated with a 2D equidistant lattice that has the spatial resolution later on used in the ADDA simulations. The lattice parameter was given by the ratio of the simulated wavelength λ and the desired dipole per wavelength (dpl) resolution. Each of the points of the 2D lattice was filled equidistantly in the third dimension to the



interpolated height present at that point, as shown in the centre image of figure 3. This created a bulk 3D model of the chromosome. The porosity of the chromosome is represented by the effective index of 1.4. Due to the challenging aspect ratio of the chromosomes, which are up to $8 \mu\text{m}$ in length, about $1 \mu\text{m}$ in width and only $0.07 \mu\text{m}$ in height, the discretisation in the latter dimension was rather coarse. With 100 dipoles per wavelength, the corresponding spatial resolution was 5.43 nm and about 3.5 million dipoles needed to be calculated.

2.4.2. ADDA simulations

The experimental conditions were replicated in the ADDA simulations. Therefore, a non-polarised, monochromatic plane wave with a wavelength of 543 nm and an incident angle θ_0 of 121° was used. For all ADDA simulations, the conjugate gradient method (Barrett *et al* 1994) (CGNR) was chosen as iterative solver, for its monotonic convergence and robustness. To obtain an overview of the angular scattering pattern of the chromosomes, scattering angles θ from 0° to 180° in combination with azimuthal angles ϕ from 0° to 360° were calculated in one degree steps. Each angle pair resulted in a Mueller matrix, describing the scattering event under this angle for arbitrary polarisation. Hence, the polarisation of the illumination and polarisation effects of other system components, like the cover glass, could be regarded post simulative via Stokes formalism.

2.4.3. Post simulation data processing

To correlate the simulation data with the measurements, the observable solid angle, defined by the objective and the surrounding medium of the scatterer, had to be identified in the simulation data. Since the surrounding medium was air, the incident angle as well as the objectives acceptance angle were conserved. A selection condition was derived from a rotation by θ_0 to translate the angles θ and ϕ from the ADDA coordinate system to the setup system leading to

$$\cos(\theta_0) \cdot \cos(\theta_j) - \sin(\theta_0) \cdot \sin(\theta_j) \cdot \sin(\phi_j) > \cos(\theta_{acc}). \quad (1)$$

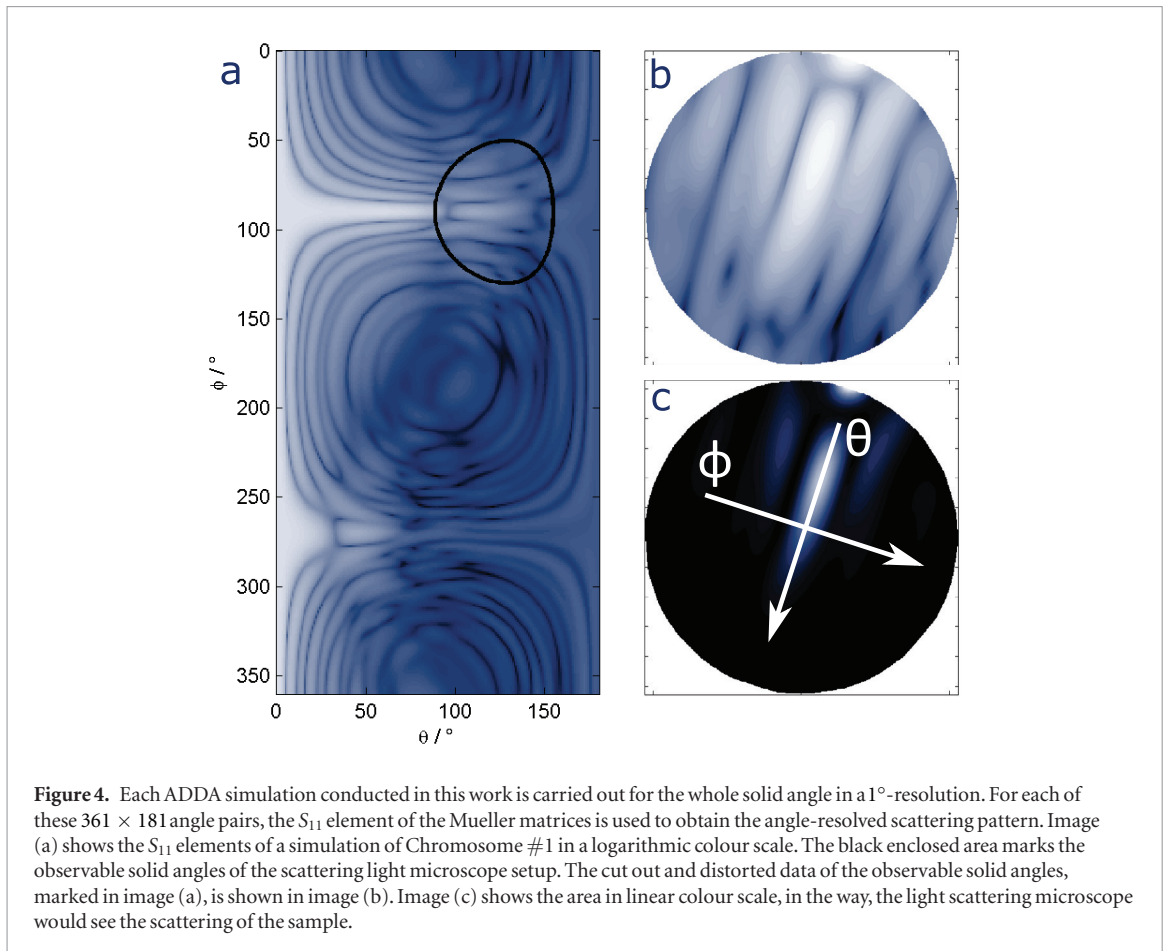
The angle pairs (θ_j, ϕ_j) satisfying equation (1) were considered inside the observable solid angle. This results in the circular observable solid angle, visualised in figure 4. Since the incident azimuthal angle ϕ_0 results merely in a rotation of the circular observable solid angle, it has no influence on the observability of an angle pair (θ_j, ϕ_j) .

The incident light S_{in} as well as the scattered light had to pass through the cover glass during measurements. This was modelled using the Stokes formalism

$$S_{\text{out},j} = T_{2,j}^2 \cdot R_{2,j} \cdot M_j \cdot R_{1,j} \cdot T_1^2 \cdot S_{\text{in}}. \quad (2)$$

The index j describes the polar- and azimuthal angle pair of the ADDA simulation results and therefore different light paths. The influence on the light properties, described by Fresnel refraction, is represented by the transmission matrices T which is defined in equations (3)–(6) in accordance with Fresnel refraction in the Mueller–Stokes formulation (Collett 1971)

$$T = \begin{pmatrix} t_{\perp} + t_{\parallel} & t_{\perp} - t_{\parallel} & 0 & 0 \\ t_{\perp} - t_{\parallel} & t_{\perp} + t_{\parallel} & 0 & 0 \\ 0 & 0 & 2\sqrt{t_{\perp}t_{\parallel}} & 0 \\ 0 & 0 & 0 & 2\sqrt{t_{\perp}t_{\parallel}} \end{pmatrix} \quad (3)$$



with

$$t_{\perp} = \frac{\tan(\alpha)}{\tan(\beta)} \left(\frac{2\sin(\beta)\cos(\alpha)}{\sin(\alpha + \beta)} \right)^2 \quad (4)$$

$$t_{\parallel} = \frac{\tan(\alpha)}{\tan(\beta)} \left(\frac{2\sin(\beta)\cos(\alpha)}{\sin(\alpha + \beta)\cos(\alpha - \beta)} \right)^2 \quad (5)$$

$$\beta = \arcsin \left(\frac{n_2}{n_1} \sin(\alpha) \right). \quad (6)$$

The angle α describes the angles of the light path, towards the surface normal of the interface before the Fresnel refraction. β denotes the respective angle after the event. The refractive index n_1 belongs to the medium, the light originates from, while n_2 belongs to the medium, the light enters.

Since the measurements on the chromosomes were conducted in air, both cover glass surfaces were in contact with the same material. Thus, the only difference between the calculation of the passage of the first interface, to the passage of the second one, is that α and β are interchanged. In equations (4) and (5) α and β only occur as a sum or as difference in the argument of a cosine. In both cases, α and β are interchangeable, rendering a discrimination between the passage of the first or the second interface obsolete

$$T_{i,2} \cdot T_{i,1} = T_i^2. \quad (7)$$

Additionally, the first transmission is independent from the scattering angle pairs (θ_j, ϕ_j) since the scattering has yet to occur. The influence of transmissions after multiple reflections inside the cover glass was considered insignificant and therefore neglected.

Whenever scattering, refraction or reflection occurs, the polarisation has to be translated into parallel and perpendicular polarisation in respect to the plane, in which the respective event takes place (Bohren and Huffman 2008). Scattering planes are defined by the incident wave vector \vec{k}_i and the scattered wave vector \vec{k}_s , while the plane in which Fresnel refraction takes place is defined by \vec{k}_i and the interface normal \vec{n} . The translations of the polarisations can be realised through rotation matrices R

$$R = \begin{pmatrix} 1 & 0 & 0 & 0 \\ 0 & \cos(2\chi) & \sin(2\chi) & 0 \\ 0 & -\sin(2\chi) & \cos(2\chi) & 0 \\ 0 & 0 & 0 & 1 \end{pmatrix}. \quad (8)$$

The angles χ can be determined from the arc cosine of the inner product of the plane the polarisations are defined in and the one the next event takes place

$$\chi_i = \arccos(\vec{n}_{i-1} \cdot \vec{n}_i). \quad (9)$$

After the first transmission through the cover glass and the first translation of polarisations, the scattering event occurred. This was described by the Mueller matrices M_j , obtained from the ADDA simulations. In the present work, the polarisation of $S_{out,j}$ was not of interest. Therefore only their first element S_1 , holding the parameter proportional to the intensity was evaluated. Note, that even in this case it is important to consider polarisations during the applications of the transmission matrices T . Equation (3) shows the influence of the polarisations on the S_1 element clearly.

At this point, the azimuthal incident light angle ϕ_0 , depicted in figure 1 was applied to the simulation data, resulting in the angle between the θ -direction and the vertical, visible for example in the right images of figure 4. Subsequently, the simulation data was interpolated onto a 400 by 400 grid and normalised in the same way the light scattering measurement data was. Furthermore, a metric was needed to qualify the similarity between simulation and actual measurement. Thus simulations were correlated with the measurements in two dimensions using the Matlab function `corr2()`, following the Pearson correlation (Pearson 1895)

$$\text{corr2}(A, B) = \frac{\sum_m \sum_n (A_{mn} - \bar{A})(B_{mn} - \bar{B})}{\sqrt{\left(\sum_m \sum_n (A_{mn} - \bar{A})^2\right) \left(\sum_m \sum_n (B_{mn} - \bar{B})^2\right)}}. \quad (10)$$

2.4.4. ADDA model orientation

One major influence on the angular scattering pattern, when studying complex scatterer geometries, is their orientation. Even slight deviations between the experimental orientation and the one assumed in the simulation can have a significant impact on the angular intensity distributions. Therefore, the correlation between simulation and measurement is strongly dependent on the orientation parameters chosen for the ADDA simulations. Even more so for larger single scatterers, with higher frequencies in their angular scattering pattern. This strong dependency makes it important to use fine steps, when varying orientation of the scatterer relative to the incident light in search for a good correlation, resulting in a larger number of simulations needed. In the present work, uncertainties in the alignment of the chromosome in the experimental setup and the manual selection of the long axis of the simulation model contribute to this issue.

The first step to solving this problem was to define a range, which describes the uncertainty of scatterer orientation. This was assumed to be $\pm 5^\circ$ in all three rotations needed to describe an orientation in ADDA. These rotations will be referred to as X , Y , and Z , according to the rotations of the geometrical model used in the ADDA simulations around the model axes x , y , and z , as defined in the right image of figure 3. In a second step, the resolution had to be determined in which the highest correlation was to be searched. A 0.5° resolution was assumed sufficient. The brute force approach would have been to conduct ADDA simulations for all combinations of 21 values of X , Y , and Z , resulting in $21^3 = 9261$ simulations, of which each takes 30–60 min on a desktop computer using two cores. From these simulations, a lookup-table (LUT) could have been created, consisting of scattering patterns for the different orientation deviation. Through comparison of the measurement data with the LUT, the correct orientation could have been found and the correlation between measurement and simulation determined.

Due to the immense computational effort the brute force approach would cost, a method was derived that approximates two of the three rotations, namely X and Y , with an angular shift of θ and ϕ in the angular scattering pattern, visible in figure 4. θ and ϕ were therefore used as approximation parameters for X and Y . This reduced the dimensions of the LUT that have to be simulated with ADDA from three to one. In the present work, this corresponds to a reduction of necessary ADDA simulations from 9261 to 21, which is more than two orders of magnitude. Twenty additional ADDA simulations are necessary to obtain the translation matrix C that allows the translation from the approximation parameters θ and ϕ back to the rotations X , Y , and Z , used in the ADDA simulations

$$\begin{pmatrix} X \\ Y \\ Z \end{pmatrix} = C \begin{pmatrix} \theta \\ \phi \\ \tilde{Z} \end{pmatrix}. \quad (11)$$

\tilde{Z} represents the ADDA simulations used to create the LUT in combination with the θ/ϕ -shift approximation. It is noted differently from Z to stress its belonging to the parameters used to create the LUT in contrast to the rotations X , Y , and Z that are used in ADDA simulations.

Since the LUT created with the θ/ϕ -shift does not consist of actual numerical light scattering simulations, but of approximations, it was used to provide an initial guess for a very confined set of ADDA simulations. For the confined set, a deviation in X , Y , and Z of $\pm 0.5^\circ$ was assumed. One step in each rotation direction was found to be enough to secure the initial guess was correct with an accuracy of $\leq 0.5^\circ$ to create a grid of misalignments. Thus an additional $3^3 = 27$ ADDA simulations of rotations, starting from the guess values were conducted. The orientation of the ADDA model was determined by comparison between the measurements and the mentioned 27 ADDA simulations. It was found that a step size of 1° was sufficient to achieve a guess accuracy of $\leq 0.5^\circ$, reducing the ADDA simulations necessary for \tilde{Z} from 21 to 11. Therefore the total of ADDA simulations needed adds up to 58 instead of 9261, still reducing the number of simulations needed by a factor of 160 and saving time by the same amount.

Parameter restriction with a fast, but coarse method followed by a slower, but more precise one has been applied to biological samples before (Ho *et al* 2015). Light scattering data was first analysed with continuous wavelet transform inverse light scattering analysis (CWT ILSA) to predetermine the filter cutoff frequency and a diameter prediction for a subsequent Mie theory based ILSA, reducing the overall analysis time significantly.

3. Results and discussion

The angular scattering pattern is dependent on parameters such as the illumination wavelength and beam shape on the one hand and on the other hand on the refractive index, size and shape of the studied scatterer as well as its orientation. The influence of the last parameter is shown in the following subsection and a method is derived to approximate variations in the studied scatterers orientation. This method is then used in the evaluation of the chromosome measurements and simulations, which are discussed in the second part of this section.

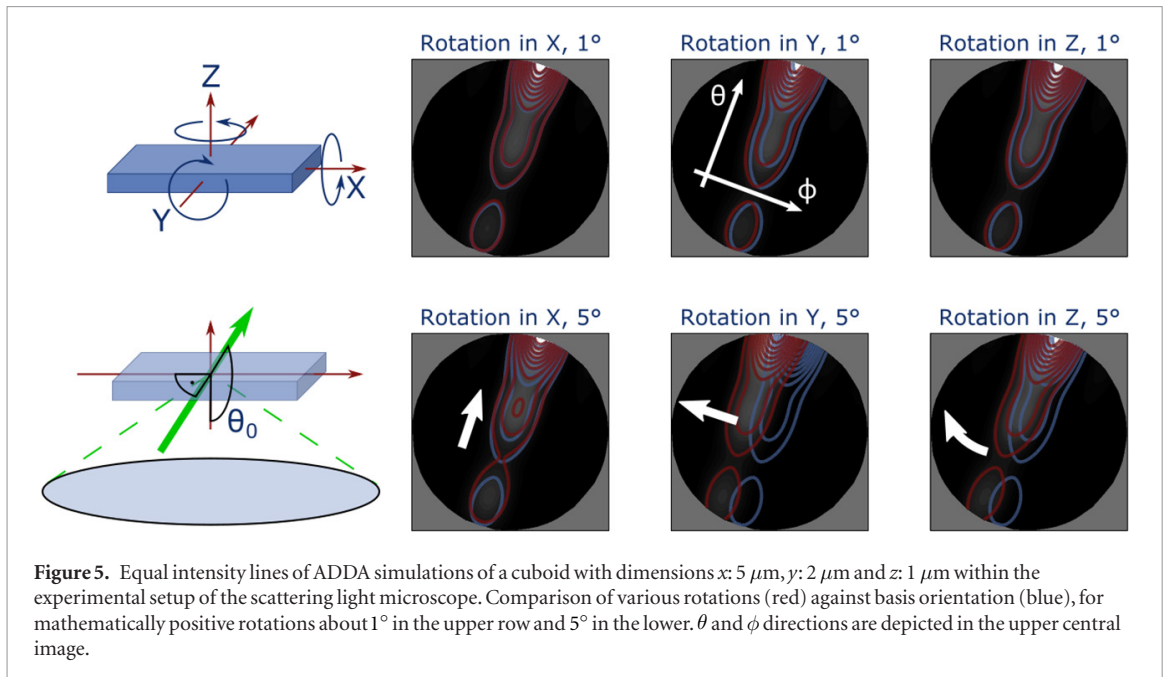
3.1. θ/ϕ -shift method

This subsection deals with the influence of a scatterers misalignment on its scattering pattern. After a short study that shows the impact and regularities of the effect those misalignments have on the scattering patterns, the way to derive the θ/ϕ -shift method is presented, validated in a test study with ADDA simulations and certain characteristics are discussed.

To study the influence of the tip, tilt, and rotation in the object plane of the sample on the angular scattering patterns several simulations were performed. As simple test structure, a cuboid with dimensions comparable to those of chromosomes was chosen. The cuboid was generated with a refractive index of 1.4, a length $5 \mu\text{m}$, a width $2 \mu\text{m}$, a height $1 \mu\text{m}$, and with a dipole resolution of 40 nm. The angle-resolved light scattering of this cuboid was simulated using ADDA for different orientation deviations. These deviations could be described by linear independent rotations starting from a defined basis orientation. For convenience, the axes of the Cartesian coordinate system in which the scatterer was defined were used, as shown in the upper left of figure 5. The orientation deviations of the scatterer around the x -, y -, and z -axis will be referred to as X , Y , and Z . The basis orientation used here reproduced the position of a sample on a cover glass in the scattering light microscope and is shown in the lower left of figure 5. For the first set of simulations the cuboid was rotated by 1° around each axis independently. In the second set the rotation, starting from the basis orientation, was increased to 5° . The ADDA simulations were carried out with a non-polarised, monochromatic plane wave illumination possessing a wavelength of $1 \mu\text{m}$, for convenience. The results show a high sensitivity of the setup to the sample orientation. Even changes of one degree are easily visible in the scattering pattern, as shown in the upper row of figure 5.

Several regularities can be observed in figure 5. A positive rotation of the sample in X , shown in the left images of figure 5, resembles a shift of the scattering pattern towards lower polar angles θ , which corresponds to the upper right side in the images. At times, this shift might distort the visualisation of the scattering pattern, which is an artefact of the normalisation of the intensities inside the observable area and will be discussed later on. Positive rotations in Y , presented in the centre images of figure 5 behave similarly to a shift of the observable solid angle towards lower azimuthal angles ϕ . Orientation variation of the model in the objective plane, which is Z , rotates the scattering pattern around a point outside the observable area.

These observed regularities motivate the approximation of scatterer misalignment (X , Y , Z) inside the ADDA simulations by a shift of the angular scattering pattern (shown in figure 4(a)) in θ and ϕ , which will be referred to as approximation parameters. Since the rotation in Z resulted in a rotation of the scattering pattern inside the observable area, instead of a shift, this parameter remained directly simulated in ADDA. To complete the approximation parameter space, $\tilde{Z} = Z$ was introduced as the third approximation parameter. The goal was to find a matrix C that translates the approximation parameters θ , ϕ , and \tilde{Z} back to the ADDA model rotations X , Y ,



and Z , as shown in equation (11). These orientation parameters could be used as initial guess for a very confined set of ADDA simulations.

Since the direct approach to determine the relations $X(\theta, \phi, \tilde{Z})$, $Y(\theta, \phi, \tilde{Z})$ and $Z(\theta, \phi, \tilde{Z})$, and therefore C , would have needed a large amount of ADDA simulations, $\theta(X, Y, Z)$, $\phi(X, Y, Z)$ and $\tilde{Z}(X, Y, Z)$ were analysed instead. Therefore a test set of scattering patterns for various scatterer misalignments was produced from ADDA simulations. Additionally, a lookup table $L(\theta, \phi, \tilde{Z})$ was created using the shift in θ and ϕ . Comparison between the test set and the LUT resulted in the relations $\theta(X, Y, Z)$, $\phi(X, Y, Z)$ and $\tilde{Z}(X, Y, Z)$, for the approximation parameters yielding the best approximation to the scattering pattern from the test set.

Thus a test set of ADDA simulations was constructed that represented a scatterer with various orientation deviations X , Y , and Z in regard to the basis orientation. The generic cuboid described before was rotated from -5° to 5° in 1° steps in each rotation X , Y , and Z independently, creating three sets of 11 angular scattering patterns. The lookup table $L(\theta, \phi, \tilde{Z})$ was created with a larger range of -7° to 7° in 1° steps in θ , ϕ , and \tilde{Z} . This was done, because of the unknown elements of the matrix C , it was possible that the approximation of a rotation of 5° in X , Y or Z would need larger θ or ϕ shifts than 5° . Therefore, the resulting LUT $L(\theta, \phi, \tilde{Z})$ held $15^3 = 3375$ scattering patterns, obtained from one ADDA model and 15 ADDA simulations, belonging to the \tilde{Z} rotations. Comparison between each scattering pattern from the test set, obtained through ADDA simulations, with the approximation LUT yielded the relation between the approximation parameters with the best fitting scattering patterns to those from the ADDA rotations $\theta(X, Y, Z)$, $\phi(X, Y, Z)$ and $\tilde{Z}(X, Y, Z)$. The results are shown in the left column of figure 6, marked with crosses.

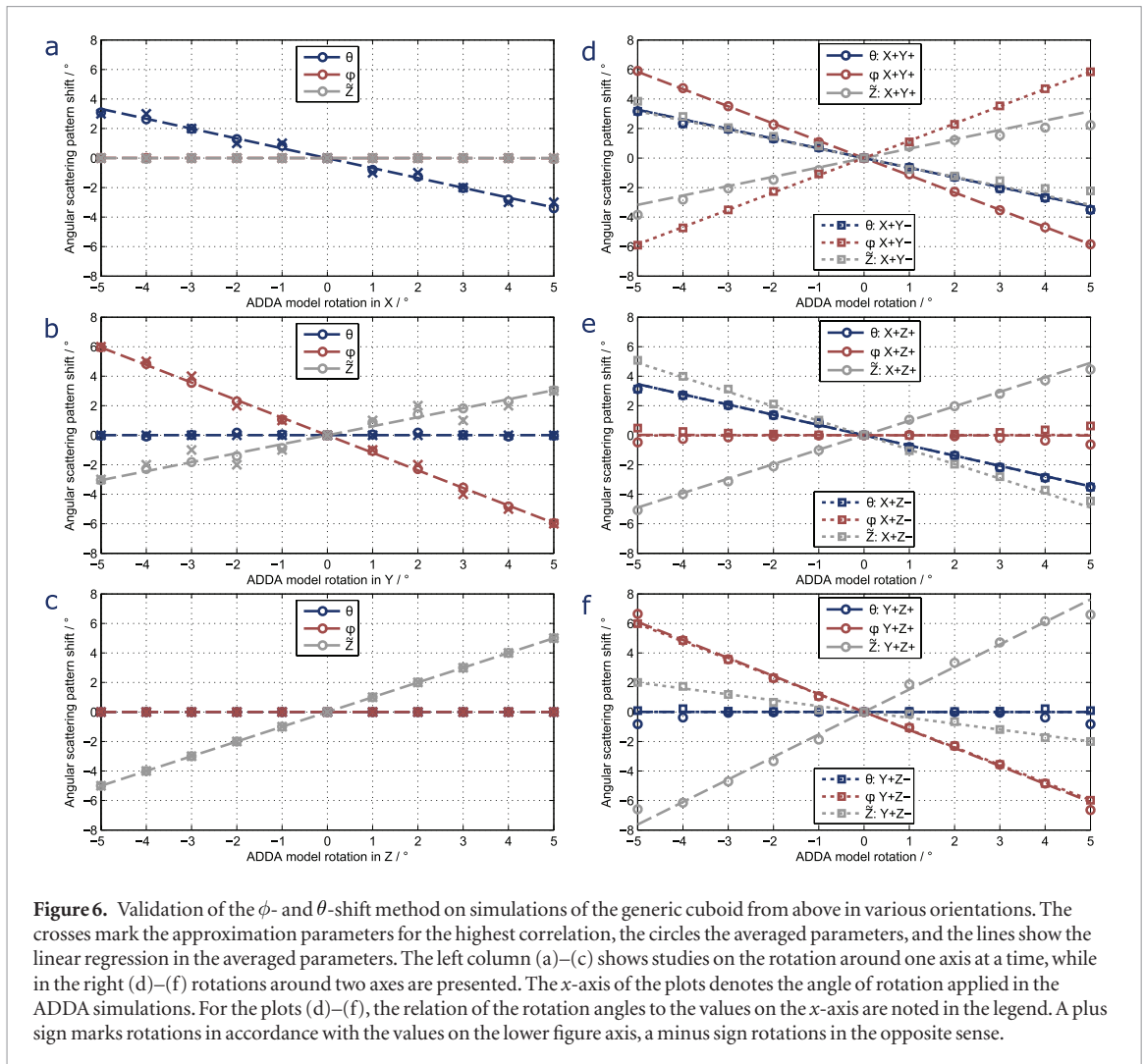
Due to the discrete nature of LUT parameters, only the predefined parameters were possible outcomes for θ , ϕ and \tilde{Z} . With a resolution of 1° in three dimensions, it is rather improbable that the centre for the highest correlation falls on a combination of the predefined parameters of the LUT. To enable this method to take a value for parameter suggestions outside the given discrete values, an average between the parameters with the highest correlations to the test set was formed. A normalised weighting equation was constructed that increases rapidly for correlation values c_i of 1

$$w_i = \frac{\frac{1}{1-c_i}}{\sum_j \frac{1}{1-c_j}}. \quad (12)$$

Each component of the average was weighted with respect to their correlation value c_i , as described in equation (12). The weighted average was performed on the approximation parameters of the seven highest correlations, one for the highest correlation and two for each dimension of the LUT

$$\begin{pmatrix} \theta_{\text{av}} \\ \phi_{\text{av}} \\ \tilde{Z}_{\text{av}} \end{pmatrix} = \sum_i w_i \cdot \begin{pmatrix} \theta_i \\ \phi_i \\ \tilde{Z}_i \end{pmatrix}. \quad (13)$$

If by chance, or by design, a parameter set results in a perfect correlation, this parameter set is obtained, regardless of the other outcomes. For a correlation value of 1, w_i becomes 1. Since the weighting function described in



equation (12) is normalised, all other weights result in 0. This is the case for the base orientation with 0° shift or rotation in figure 6. For each averaged set of parameters, an averaged correlation c_{av} has been calculated in the same manner, as presented in equation (14)

$$c_{av} = \sum_i w_i \cdot c_i. \quad (14)$$

This correlation decreases for shift and rotation angles over 3 degrees. The assumption was made that c_{av} is an indicator for the quality of the found averaged approximation parameters. Therefore, the linear regression shown in figure 6 is also weighted. The weights for each data point were determined as described in equation (12), but with the averaged correlation c_{av} values instead of c_i .

In case of the simple model of a cuboid, the linear assumption yields satisfying results for small rotations. The results for X variation of the ADDA model are shown in figure 6(a). As observed in figure 5, only a shift in θ occurs. Image (b) of the same figure presents the results for the Y -rotation. This produces a response in two of the approximation parameters, ϕ and \tilde{Z} . Since the effect of the approximation parameter \tilde{Z} is obtained through ADDA simulations around Z , it seems, rotations appear for Y -rotations, which have to be compensated by including a change in \tilde{Z} . This has to be considered for the inverse problem, when the actual model rotations are to be derived from the approximation parameters. Image (c) of figure 6 shows the approximation parameters for a model rotation Z . Since \tilde{Z} is produced through ADDA simulations with a misalignment in Z , the actual test patterns are present in the approximation LUT and therefore the natural outcome of the correlation. Still, it is important to verify that there is no interference of the other two approximation parameters with this correlation. From these results, the orientation deviations in the ADDA simulations should be accessible through the approximation parameters with the fitted parameter m_{ij} denoting the slope of the linear regression in the approximation parameter i for a rotation of the ADDA model around j .

Since scatterers in real experiments do not constrain themselves to a rotation around a single axis, the study was expanded on rotations around two axes. The scatterer was rotated around both axes by the same amount, once in the same rotational sense, once in the opposed. The results are shown in figure 6, images (d)–(f). A strong

Table 1. Slope values corresponding to the linear regressions in figure 6. For the last two rows, marked with *, the parameter space in \tilde{Z} was increased to $[-8^\circ, 8^\circ]$ since the approximation parameters could not take the value, predicted by the linear regression, as visible in figure 6(f).

Rotation	m_θ	m_ϕ	$m_{\tilde{Z}}$
X	-0.67 ± 0.01	0.00 ± 0.00	0.00 ± 0.00
Y	0.00 ± 0.01	-1.19 ± 0.01	0.61 ± 0.02
Z	0.00 ± 0.00	0.00 ± 0.00	1.00 ± 0.00
X + Y +	-0.65 ± 0.01	-1.17 ± 0.01	0.63 ± 0.05
X + Y -	-0.65 ± 0.01	1.17 ± 0.01	-0.63 ± 0.05
X + Z +	-0.69 ± 0.01	0.00 ± 0.03	0.98 ± 0.02
X + Z -	-0.69 ± 0.01	0.00 ± 0.03	-0.98 ± 0.02
Y + Z +	0.00 ± 0.05	-1.22 ± 0.03	1.53 ± 0.06
Y + Z -	0.00 ± 0.01	-1.19 ± 0.01	-0.40 ± 0.02
Y + Z + *	0.00 ± 0.03	-1.21 ± 0.02	1.64 ± 0.05
Y + Z - *	0.00 ± 0.01	-1.19 ± 0.01	-0.40 ± 0.02

sign for independence of the single rotations is the consistency of the slopes, for rotations in the same direction and the ones with opposed directions of rotation. If superposition is assumed, the responses would enhance one another in the one combination of rotations and attenuate each other in the opposite combination. The values of the slopes are listed in table 1. Model orientations consisting of XY or XZ show a high consistency with the rotations around the individual axis. They produce the same slopes as the individual X, Y, and Z rotations, shown in figures 6(a)–(c), within the margin of error. The slope errors Δm for a linear fit in N data points are determined with

$$\Delta m = \sqrt{\frac{N}{N-2} \frac{\sum_i^N ((y_i - \bar{y}) - m(x_i - \bar{x}) - c)^2}{\sum_i^N (x_i - \bar{x})^2}}. \quad (15)$$

The fit function was defined as $y = mx + c$. Since this approach yielded an offset c of 0 in all cases, only the slopes m are used from here on. The variables x_i and y_i describe the values from corresponding ADDA model rotations X, Y, Z and approximation parameters θ , ϕ , \tilde{Z} . Averages are denoted by a bar over the variable, such as \bar{x} and \bar{y} .

As observed before, a Y-rotation produces ϕ and \tilde{Z} responses. Therefore, the rotation pair YZ, presented in figure 6(f) is of special interest. The slopes $m_{\tilde{Z},YZ}$ are clearly not equal for the different directions of rotation. In the case of matching rotations in Y and Z, the absolute value of the slope is larger than in the opposite case. This is to be expected, if a superposition of the \tilde{Z} response caused by the Z-rotation and the one caused by the Y-rotation is assumed. In that case, the slopes produced by the Z-rotation $m_{\tilde{Z},Z+}$ and $m_{\tilde{Z},Z-}$ should be extractable

$$\begin{aligned} m_{\tilde{Z},Y+Z\pm} &= m_{\tilde{Z},Y+} + m_{\tilde{Z},Z\pm} \\ m_{\tilde{Z},Z+} &= m_{\tilde{Z},Y+Z+} - m_{\tilde{Z},Y+} = 1.64 \pm 0.05 - 0.61 \pm 0.02 = 1.03 \pm 0.05 \\ m_{\tilde{Z},Z-} &= m_{\tilde{Z},Y+Z-} - m_{\tilde{Z},Y+} = -0.40 \pm 0.02 - 0.61 \pm 0.02 = -1.01 \pm 0.03. \end{aligned} \quad (16)$$

Within the margin of error, the slope $m_{\tilde{Z},Z}$ from the YZ-rotation study are fitting nicely with the slopes obtained from the isolated Z-rotation and the XZ-rotations, shown in table 1. Since the approximation parameter range was limited to $[-7^\circ, 7^\circ]$, the outer \tilde{Z} values in figure 6(f) could not reach the values predicted by the slope of the fit. With a larger parameter range, increased to $[-8^\circ, 8^\circ]$ for \tilde{Z} , the slope $m_{\tilde{Z},Y+Z+}$ changed from 1.53 ± 0.06 to 1.64 ± 0.05 .

In conclusion of this section, linearity in the dependence of the approximation parameters and the actual rotations in the simulation can be assumed for small angles of rotation. Additionally, the actual rotations needed in the ADDA simulation to resemble the θ - and ϕ -shift can be obtained. The translation matrix for this is presented in equation (20)

$$\theta(X) = m_{\theta,X} \cdot X \quad (17)$$

$$\phi(Y) = m_{\phi,Y} \cdot Y \quad (18)$$

$$\tilde{Z}(Y, Z) = m_{\tilde{Z},Y} \cdot Y + m_{\tilde{Z},Z} \cdot Z \quad (19)$$

$$\Rightarrow \begin{pmatrix} X \\ Y \\ Z \end{pmatrix} = \begin{pmatrix} \frac{1}{m_{\theta,X}} & 0 & 0 \\ 0 & \frac{1}{m_{\phi,Y}} & 0 \\ 0 & -\frac{m_{\tilde{Z},Y}}{m_{\tilde{Z},Z}} \frac{1}{m_{\phi,Y}} & \frac{1}{m_{\tilde{Z},Z}} \end{pmatrix} \cdot \begin{pmatrix} \theta \\ \phi \\ \tilde{Z} \end{pmatrix}. \quad (20)$$

Table 2. θ , ϕ and \tilde{Z} responses to isolated rotations around X, Y, and Z for various scatterer geometries. $m_{i,j}$ denotes the response relation between the approximation parameter i and the model rotation j .

Model	$m_{\theta,X}$	$m_{\phi,Y}$	$m_{\tilde{Z},Y}$	$m_{\tilde{Z},Z}$
Cuboid #1	-0.67 ± 0.01	-1.19 ± 0.01	0.61 ± 0.02	1.00 ± 0.00
Cuboid #2	-1.00 ± 0.04	-1.19 ± 0.01	0.61 ± 0.01	1.00 ± 0.00
Cuboid #3	-1.43 ± 0.03	-1.18 ± 0.01	0.61 ± 0.01	1.00 ± 0.00
Chromosome #1	-1.79 ± 0.04	-1.20 ± 0.01	0.59 ± 0.01	1.00 ± 0.00
Chromosome #2	-1.67 ± 0.07	-1.19 ± 0.01	0.59 ± 0.02	1.00 ± 0.00
Chromosome #3	-1.64 ± 0.06	-1.19 ± 0.01	0.60 ± 0.02	1.00 ± 0.00
Chromosome #4	-1.68 ± 0.07	-1.19 ± 0.01	0.59 ± 0.02	1.00 ± 0.00
Chromosome #5	-1.66 ± 0.07	-1.20 ± 0.01	0.58 ± 0.02	1.00 ± 0.00
Chromosome #6	-1.73 ± 0.09	-1.19 ± 0.01	0.60 ± 0.02	1.00 ± 0.00

3.1.1. Chromosomes

The θ/ϕ -shift method was applied to the chromosome simulations to reduce the amount of simulations needed to identify the best-fitting chromosome model. For each chromosome model, the routine as described above for the single axis rotations has been performed to obtain the slopes $m_{\theta,X}$, $m_{\phi,Y}$, $m_{\tilde{Z},Y}$ and $m_{\tilde{Z},Z}$. The range of approximation parameters was reduced to -5° to 5° in 1° steps for θ , ϕ and \tilde{Z} . The slopes achieved are listed in table 2.

The response of \tilde{Z} on pure Z-rotations is not disturbed by any scatterer geometry and remains constantly 1.00. The responses of \tilde{Z} and ϕ on Y-rotations seem rather independent of the scatterer geometry, as presented in table 2. The θ values for the isolated X-rotation, on the other hand, are distinctively not constant. To study this effect, two additional cuboids have been simulated. The slopes seem to decrease with a rising aspect ratio between width (y -direction) and height (z -direction) in a non-linear manner. The sizes and aspect ratios are shown in table 3. A second feature of the X-rotation is its effect on the image, taken from the observable solid angle. As shown in figure 5, the X-rotation of the model results in a shift in θ -direction, thereby removing the highest, or adding higher intensity values to the observable area. Through normalisation, this can change the intensities of the whole area. It is, however, changing all intensities by the same normalisation factor k . Replacing the image data A from equation (10) with $k \cdot A$ yields no different correlation to the image B . Therefore, the intensity gradients around the maximum, near the border of the observable solid angle in θ -direction, is of no significance to the variation of intensities when shifting θ .

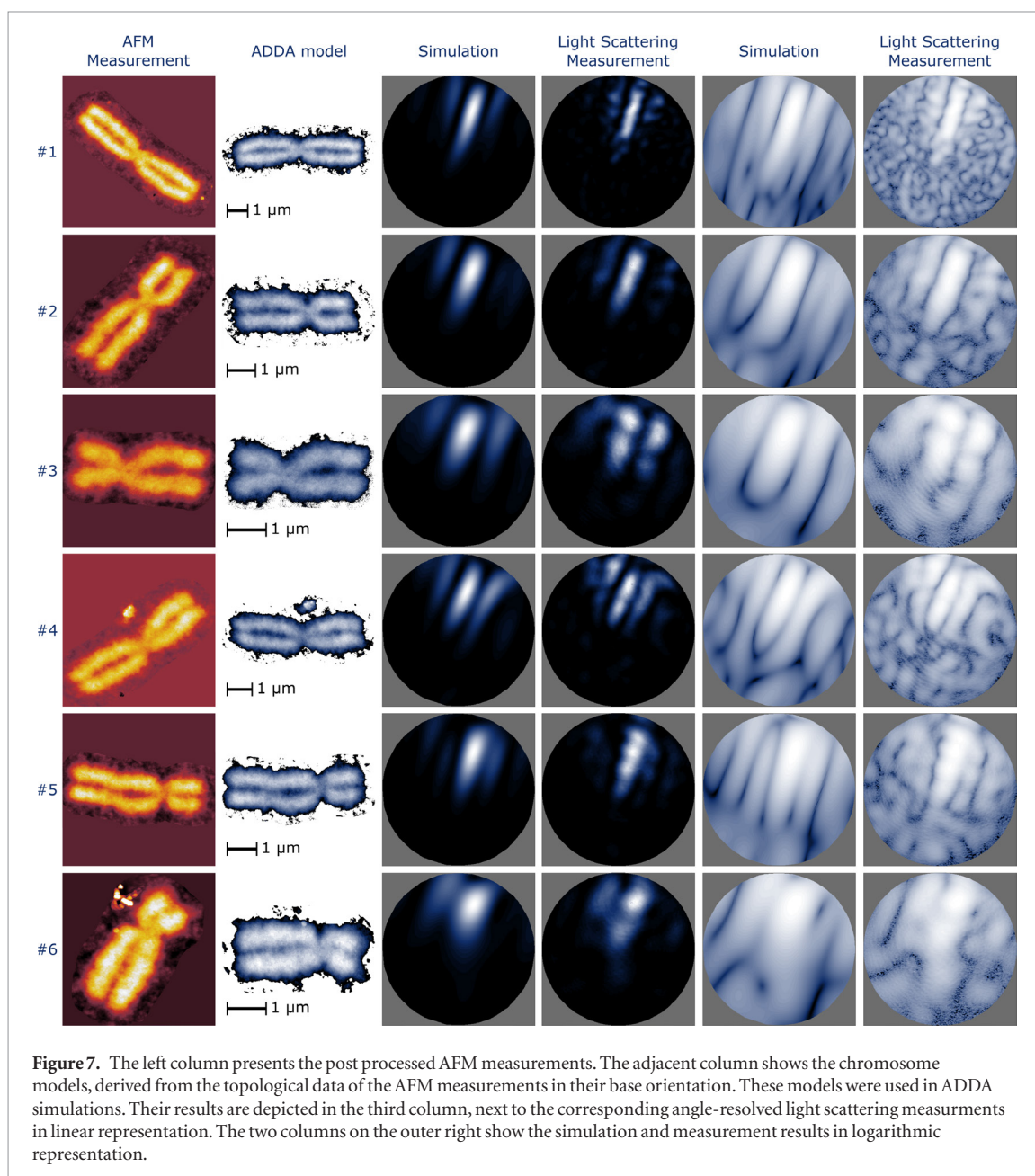
With the θ, ϕ, \tilde{Z} -lookup table ready, the light scattering measurement data for each chromosome was correlated with the LUT. As before, the weighted average of the approximation parameters corresponding to the seven highest correlations was formed. These parameters were translated into the actual rotation values via equation (20). Starting from this model orientation, combinations of variations of 0.5° in each direction were performed, resulting in 27 ADDA simulations per chromosome. From those simulations, the one with the highest correlation to the measurement was chosen. The corresponding results are shown in figure 7. In all 6 cases, the ADDA simulation with the initial guess parameters of the θ/ϕ -shift method yielded the highest correlation in comparison to the 26 surrounding ADDA simulations. This hints towards a guess parameter accuracy better than 0.5° .

In general, the simulation results fit the measurements remarkably well. The logarithmic representation shows high similarities in the scattering patterns even in areas with low intensities. This is of special importance, since these areas did not contribute significantly to the correlation result, thereby having little effect on the determination of the orientation parameters. High similarity in these areas show that the simulation conditions match the measurement conditions well, even beyond the ‘fitted’ areas. The light scattering measurements show patterns along the θ -direction, which are not present in the simulation results. One possible explanation are irregularities, like dust and organic matter, of unknown optical properties, surrounding the chromosomes during the measurement. During measurements the chromosomes were positioned in a circular field of view, cut by a pinhole. The debris mentioned above would be generally located beside the chromosome, artificially enlarging the width of the scatterer. Thus introducing higher frequencies in the angular scattering patterns in θ -direction than there should be, if the chromosome was completely isolated.

The correlation between scatterer dimensions and frequencies in the angular scattering pattern is observable in the ADDA simulations, where nearly no debris is included in the simulation. Since the chromosome’s width is generally a lot smaller than their length, the Fourier signal in θ -direction is relatively smooth, due to the absence of high frequencies in the angular bandwidth. The same effect is visible for short chromosomes, like #3 and #6

Table 3. Model sizes and aspect ratios of chromosomes, and cuboids used in θ/ϕ -shift method validation.

Dimension	Cuboids			Chromosomes					
	#1	#2	#3	#1	#2	#3	#4	#5	#6
Length / μm	5.00	5.00	5.00	6.26	3.86	3.16	4.82	4.22	3.02
Width / μm	2.00	2.00	3.00	1.55	1.23	1.25	1.88	1.38	1.37
Height / μm	1.00	0.50	0.50	0.09	0.08	0.09	0.09	0.08	0.08
Aspect ratio $\frac{W}{H}$	2.00	4.00	6.00	17.81	15.07	14.38	21.62	18.14	18.07
Aspect ratio $\frac{L}{H}$	5.00	10.00	10.00	72.00	47.33	36.37	55.44	55.50	39.71
Aspect ratio $\frac{L}{W}$	2.50	2.50	1.67	4.04	3.14	2.53	2.56	3.06	2.20



in ϕ -direction. Hence, the measurement could be freed of some of the influence of the surrounding debris by Fourier filtering, only allowing frequencies in θ - and ϕ -directions that correspond to either a size estimate of the measured chromosome from microscope images or the dimensions of the ADDA model, it is compared with.

Another indicator pointing towards the overlaying signal originating from the surrounding debris is the used pinhole size. Assuming the presented explanation is valid, the angular bandwidth of the overlaying patterns should increase with increasing pinhole size, since the signals from a larger area are recorded. A pinhole with a diameter of 600 μm was used for the measurement of chromosome #1, 300 μm for chromosomes #2, #4, and

Table 4. Correlation values between all measurements and simulations. For corresponding Fisher confidence intervals see table 5.

Simulations	Measurements					
	#1	#2	#3	#4	#5	#6
#1	0.934	0.949	0.754	0.842	0.912	0.850
#2	0.835	0.954	0.782	0.737	0.939	0.912
#3	0.783	0.897	0.887	0.752	0.899	0.859
#4	0.846	0.858	0.837	0.864	0.846	0.768
#5	0.852	0.911	0.783	0.775	0.968	0.874
#6	0.763	0.841	0.722	0.803	0.863	0.922

Table 5. 99.9% confidence intervals for correlations between all measurements and simulations from table 4.

Simulations	Measurements					
	#1	#2	#3	#4	#5	#6
#1	[0.932, 0.935]	[0.947, 0.950]	[0.749, 0.759]	[0.838, 0.845]	[0.910, 0.914]	[0.846, 0.853]
#2	[0.831, 0.838]	[0.953, 0.955]	[0.778, 0.787]	[0.731, 0.742]	[0.938, 0.941]	[0.910, 0.914]
#3	[0.779, 0.788]	[0.895, 0.899]	[0.884, 0.889]	[0.747, 0.757]	[0.897, 0.901]	[0.856, 0.862]
#4	[0.843, 0.849]	[0.855, 0.861]	[0.833, 0.840]	[0.861, 0.867]	[0.843, 0.850]	[0.763, 0.773]
#5	[0.848, 0.855]	[0.909, 0.913]	[0.779, 0.788]	[0.770, 0.780]	[0.967, 0.968]	[0.871, 0.876]
#6	[0.758, 0.768]	[0.837, 0.844]	[0.717, 0.728]	[0.799, 0.807]	[0.860, 0.866]	[0.920, 0.923]

#5 and the 200 μm diameter pinhole was used for chromosomes #3 and #6. The logarithmic representation shows this correlation clearly. The speckle pattern with the highest frequencies occur in the measurement of chromosome #1, were the 600 μm pinhole was used. Second to this are the measurements of chromosomes #2, #4, and #5 with the 300 μm pinhole and the smoothest speckle pattern is present in the measurements taken with the 200 μm diameter pinhole, #3 and #6.

The asymmetry of the chromosomes with shorter p-arms than q-arms carries over to the scattering pattern in both, the simulation and measurement results. This can already be observed in very rudimentary models of such chromosomes. There seems to be no direct correlation between the side the higher intensities in the scattering pattern occur and the orientation of the asymmetry during the measurement. Chromosomes #2, #5 and #6 were measured with their p-arms to the left, but the higher intensities in the resulting scattering patterns for chromosomes #2 and #6 are in the direction of lower azimuthal angles ϕ , while for chromosome #5, it appears in the direction of higher azimuthal angles.

While figure 7 only shows the correct matches between light scattering measurements and simulations, table 4 presents the numerical values for the correlations between all simulations and measurements. All measurements and ADDA models were treated equally. For each model and measurement combination, the best fitting orientation of the model was determined through the θ/ϕ -shift method. With the obtained parameters, the ADDA simulation was conducted and correlated to the measurement, ensuring the highest possible correlation for each simulation-measurement pair achievable in the evaluated range of orientations.

The Fisher confidence intervals (Fisher 1925) for Pearson correlation were calculated in accordance with the method described by Bonett and Wright (2000). The number n of correlation points was assumed $\frac{\pi}{4} \cdot 400^2$ for the circular illuminated area in the 400×400 pixel images. The 99.9% confidence intervals for each correlation value presented in table 4 have been calculated and are presented in table 5.

All chromosome simulations could be matched to their corresponding measurements through the highest correlation. In some cases, namely the simulation of chromosome #1 and the measurement of chromosome #2, the mismatched correlations are close to the matched ones. Interestingly, this is not the case the other way around, meaning, an orientation exists, where the simulation of chromosome #1 resembles the measurement of chromosome #2, but the model of chromosome #2 cannot be oriented inside the given parameter range, so that its simulation resembles the measurement of chromosome #1. Chromosome #2 and #6 stand in a similar relationship, but with the simulation of chromosome #2 being the one, fitting the measurement of chromosome #6. Would the difference between the scattering patterns only consist of a shift and would the range, in which the patterns could get shifted be large enough, table 4 would be symmetric. Thus, this effect has to be related either to the rotation \tilde{Z} or due to the limited range of $[-7^\circ, 7^\circ]$ for the approximation parameters.

Despite the similar correlation values, the correct scattering patterns can be matched with the human eye. This shows that correlation is not the ideal measure for scattering pattern similarity in this case. With an algorithm, sensitive to certain features, this method could gain in robustness. Other algorithms, such as CWS-SIM

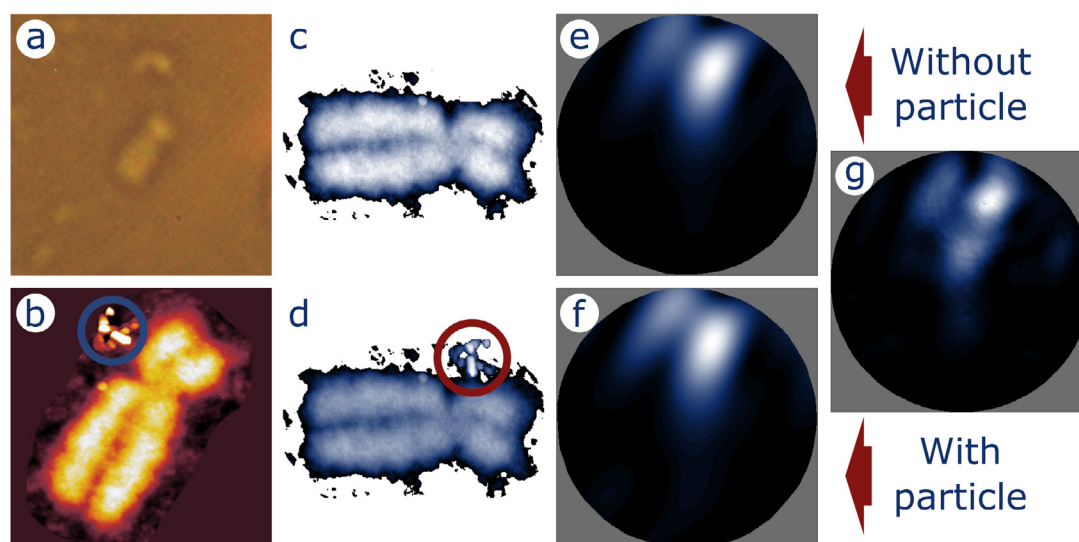


Figure 8. Chromosome #6, (a) before the light scattering measurement, (b) post processed AFM measurement, (c), (d) ADDA model without, respectively with the particle, (e), (f) post processed ADDA simulation data without, respectively with the particle and (g), the result of the light scattering measurement. All chromosome models have been treated equally. For each model-measurement pair the orientation yielding the highest correlation was determined and used.

(Sampat *et al* 2009) and Willmot (Ji and Gallo 2006), have already been studied by the authors, but offered no significant benefit.

We note that the AFM measurements of chromosome #6 show a structure next to the chromosome, near the centromere, while this structure is not present in the ADDA model. This particle found its way to that position between the light scattering and the AFM measurements. Images taken just before the light scattering measurement show no sign of a particle in the direct vicinity of the chromosome, as shown in figure 8. Chromosome #6 has been simulated with and without said particle, increasing the correlation to the measurement from 0.897 ([0.895, 0.899], 99.9% confidence interval) in the prior, to 0.922 ([0.920, 0.923], 99.9% confidence interval) in the latter case.

4. Conclusion

Human chromosomes in metaphase have been measured angularly resolved in a light scattering microscope and successfully matched to ADDA simulations of said chromosomes. The chromosomes were natural in structure, untreated with RNase or pepsin, nor were they labelled in any way. This is a first step towards using angle-resolved light scattering as a label-free method to differentiate between chromosome shapes and sizes. Furthermore, we demonstrated that numerical light scattering simulations of AFM-based geometrical models give correct predictions for angle-resolved light scattering measurements. Even small changes in the scatterer's shape are detectable, as shown in the case of chromosome #6. The influence of the particle picked up by chromosome #6 between measurements on its angle-resolved scattering pattern is significant and clearly detectable through correlation. Further investigations concerning the detectability of chromosome aberrations through angle-resolved light scattering might yield interesting results.

The linearity of the effect of small rotations of a scatterer on its angle-resolved light scattering pattern was shown in simulations on a cuboid, as well as on measurements of complex scatterer geometries in form of human metaphase chromosomes. These effects can be translated into the scatterer's orientation. A method was derived that allows correlation between simulations and measurements of complex scatterers with uncertain orientations. For an orientation parameter range with n elements, the numerical simulations needed could be reduced from $(2n + 1)^3$ to $(2n + 1) + 47$, saving computational time of the same order. An algorithm, tailored for this scenario of image similarity evaluation, could provide the association between model and measurement with an increase in robustness.

Acknowledgments

This work is financed by the Deutsche Forschungsgemeinschaft (DFG). The authors thank Prof Dr Othmar Marti for the provision of the AFM setup as well as Dominik Reitzle and Felix Glöckler for the fruitful discussions and Kirsten Reeß for the competent sample preparation.

References

- Barrett R, Berry M W, Chan T F, Demmel J, Donato J, Dongarra J, Eijkhout V, Pozo R, Romine C and Van der Vorst H 1994 *Templates for the Solution of Linear Systems: Building Blocks for Iterative Methods* vol 43 (Philadelphia, PA: SIAM)
- Bickel W and Stafford M 1981 Polarized light scattering from biological systems: a technique for cell differentiation *J. Biol. Phys.* **9** 53–66
- Bohren C F and Huffman D R 2008 *Absorption and Scattering of Light by Small Particles* (New York: Wiley)
- Bonett D G and Wright T A 2000 Sample size requirements for estimating pearson, kendall and spearman correlations *Psychometrika* **65** 23–8
- Casparsson T, Zech L, Johansson C and Modest E 1970 Identification of human chromosomes by DNA-binding fluorescent agents *Chromosoma* **30** 215–27
- Chylek P, Ramaswamy V, Ashkin A and Dziedzic J 1983 Simultaneous determination of refractive index and size of spherical dielectric particles from light scattering data *Appl. Opt.* **22** 2302–7
- Collett E 1971 Mueller–Stokes matrix formulation of Fresnel’s equations *Am. J. Phys.* **39** 517–28
- Diaspro A, Radicchi G and Nicolini C 1995 Polarized light scattering: a biophysical method for studying bacterial cells *IEEE Trans. Biomed. Eng.* **42** 1038–43
- Ding H, Wang Z, Nguyen F, Boppert S A and Popescu G 2008 Fourier transform light scattering of inhomogeneous and dynamic structures *Phys. Rev. Lett.* **101** 238102
- Donald J M, Golden A and Jennings S G 2009 Opendda: a novel high-performance computational framework for the discrete dipole approximation *Int. J. High Perform. Comput. Appl.* **23** 42–61
- Draine B T and Flatau P J 1994 Discrete-dipole approximation for scattering calculations *J. Opt. Soc. Am. A* **11** 1491–9
- Draine B T and Flatau P J 2008 Discrete-dipole approximation for periodic targets: theory and tests *J. Opt. Soc. Am. A* **25** 2693–703
- Drets M E and Shaw M W 1971 Specific banding patterns of human chromosomes *Proc. Natl Acad. Sci.* **68** 2073–7
- Drezek R A, Guillaud M, Collier T G, Boiko I, Malpica A, MacAulay C E, Follen M and Richards-Kortum R R 2003 Light scattering from cervical cells throughout neoplastic progression: influence of nuclear morphology, DNA content, and chromatin texture *J. Biomed. Opt.* **8** 7–17
- Fischer K and Schmidt M 2016 Pitfalls and novel applications of particle sizing by dynamic light scattering *Biomaterials* **98** 79–91
- Fisher R A 1925 *Theory of Statistical Estimation (Mathematical Proceedings of the Cambridge Philosophical Society* vol 22) (Cambridge: Cambridge University Press)
- Goddeeris C, Cuppo F, Reynaers H, Bouwman W and Van den Mooter G 2006 Light scattering measurements on microemulsions: estimation of droplet sizes *Int. J. Pharmaceutics* **312** 187–95
- Harrison C J, Jack E M, Allen T D and Harris R 1985 Light and scanning electron microscopy of the same human metaphase chromosomes *J. Cell Sci.* **77** 143–53
- Ho D, Drake T K, Bentley R C, Valea F A and Wax A 2015 Evaluation of hybrid algorithm for analysis of scattered light using *ex vivo* nuclear morphology measurements of cervical epithelium *Biomed. Opt. Express* **6** 2755–65
- Ji L and Gallo K 2006 An agreement coefficient for image comparison *Photogramm. Eng. Remote Sens.* **72** 823–33
- Jo Y, Jung J, Kim M H, Park H, Kang S J and Park Y 2015 Label-free identification of individual bacteria using Fourier transform light scattering *Opt. Express* **23** 15792–805
- Jo Y, Jung J, Lee J W, Shin D, Park H, Nam K T, Park J H and Park Y 2014 Angle-resolved light scattering of individual rod-shaped bacteria based on Fourier transform light scattering *Sci. Rep.* **4** 5090
- Khatibzadeh N, Stilgoe A B, Bui A A, Rocha Y, Cruz G M, Loke V, Shi L Z, Nieminen T A, Rubinsztein-Dunlop H and Berns M W 2014 Determination of motility forces on isolated chromosomes with laser tweezers *Sci. Rep.* **4** 6866
- Konokhova A I, Gelash A A, Yurkin M A, Chernyshev A V and Maltsev V P 2013 High-precision characterization of individual *E. coli* cell morphology by scanning flow cytometry *Cytometry A* **83** 568–75
- Kwon Y W, Choi D H and Jin J I 2012 Optical, electro-optic and optoelectronic properties of natural and chemically modified DNAs *Polym. J.* **44** 1191
- Lane P, Hart M, Jain V, Tucker J and Eversole J 2018 Characterization of single particle aerosols by elastic light scattering at multiple wavelengths *J. Quant. Spectrosc. Radiat. Transfer* **208** 188–95
- Lee I B, Moon H M, Joo J H, Kim K H, Hong S C and Cho M 2017 Interferometric scattering microscopy with polarization-selective dual detection scheme: capturing the orientational information of anisotropic nanometric objects *ACS Photon.* **5** 797–804
- Levsky J M and Singer R H 2003 Fluorescence *in situ* hybridization: past, present and future *J. Cell Sci.* **116** 2833–8
- Lew L N, Ting M V and Preston T C 2018 Determining the size and refractive index of homogeneous spherical aerosol particles using Mie resonance spectroscopy *Appl. Opt.* **57** 4601–9
- Lukyanchuk B S, Voshchinnikov N V, Paniagua-Domínguez R and Kuznetsov A I 2015 Optimum forward light scattering by spherical and spheroidal dielectric nanoparticles with high refractive index *ACS Photon.* **2** 993–9
- Maltsev V P 2000 Scanning flow cytometry for individual particle analysis *Rev. Sci. Instrum.* **71** 243–55
- Mie G 1908 Beiträge zur Optik trüber Medien, speziell kolloidaler Metallösungen *Ann. Phys.* **330** 377–445
- Moorhead P S, Nowell P, Mellman W J, Battips D T and Hungerford D 1960 Chromosome preparations of leukocytes cultured from human peripheral blood *Exp. Cell Res.* **20** 613–6
- Mullaney P, Van Dilla M, Coulter J and Dean P 1969 Cell sizing: a light scattering photometer for rapid volume determination *Rev. Sci. Instrum.* **40** 1029–32
- Neas D and Klapetek P 2012 Gwyddion: an open-source software for SPM data analysis *Cent. Eur. J. Phys.* **10** 181–8
- Otero F A, Frontini G L and Elicabe G E 2010 Evaluation of light scattering models to characterize concentrated polymer particles embedded in a solid polymer matrix *J. Polym. Sci. B* **48** 958–63
- Patil S R, Merrick S and Lubs H A 1971 Identification of each human chromosome with a modified giemsa stain *Science* **173** 821–2
- Pearson K 1895 Note on regression and inheritance in the case of two parents *Proc. R. Soc.* **58** 240–2
- Peelen J and Metselaar R 1974 Light scattering by pores in polycrystalline materials: transmission properties of alumina *J. Appl. Phys.* **45** 216–20
- Pencer J, White G F and Hallett F R 2001 Osmotically induced shape changes of large unilamellar vesicles measured by dynamic light scattering *Biophys. J.* **81** 2716–28
- Perelman L et al 1998 Observation of periodic fine structure in reflectance from biological tissue: a new technique for measuring nuclear size distribution *Phys. Rev. Lett.* **80** 627
- Purcell E M and Pennypacker C R 1973 Scattering and absorption of light by nonspherical dielectric grains *Astrophys. J.* **186** 705–14

- Rebner K, Ostertag E and Kessler R W 2016 Hyperspectral backscatter imaging: a label-free approach to cytogenetics *Anal. Bioanal. Chem.* **408** 5701–9
- Rothe T, Schmitz M and Kienle A 2012 Angular and spectrally resolved investigation of single particles by darkfield scattering microscopy *J. Biomed. Opt.* **17** 117006
- Sampat M P, Wang Z, Gupta S, Bovik A C and Markey M K 2009 Complex wavelet structural similarity: a new image similarity index *IEEE Trans. Image Process.* **18** 2385–401
- Santos N C and Castanho M 1996 Teaching light scattering spectroscopy: the dimension and shape of tobacco mosaic virus *Biophys. J.* **71** 1641–50
- Schmitz M, Rothe T and Kienle A 2011 Evaluation of a spectrally resolved scattering microscope *Biomed. Opt. Express* **2** 2665–78
- Seager S, Whitney B and Sasselov D D 2000 Photometric light curves and polarization of close-in extrasolar giant planets *Astrophys. J.* **540** 504
- Shemilt L, Verbanis E, Schwenke J, Estandarte A K, Xiong G, Harder R, Parmar N, Yusuf M, Zhang F and Robinson I K 2015 Karyotyping human chromosomes by optical and x-ray ptychography methods *Biophys. J.* **108** 706–13
- Stark J, Rothe T, Kieß S, Simon S and Kienle A 2016 Light scattering microscopy measurements of single nuclei compared with GPU-accelerated fdttd simulations *Phys. Med. Biol.* **61** 2749
- Stokes G G et al 1852 Xxx. On the change of refrangibility of light *Phil. Trans. R. Soc. London* **142** 463–562
- Sudarsky D, Burrows A and Pinto P 2000 Albedo and reflection spectra of extrasolar giant planets *Astrophys. J.* **538** 885
- Tamayo J 2003a Structure of human chromosomes studied by atomic force microscopy *J. Struct. Biol.* **141** 198–207
- Tamayo J 2003b Structure of human chromosomes studied by atomic force microscopy: part II. Relationship between structure and cytogenetic bands *J. Struct. Biol.* **141** 189–97
- Ushiki T and Hoshi O 2008 Atomic force microscopy for imaging human metaphase chromosomes *Chromosome Res.* **16** 383
- Wanner G, Schroeder-Reiter E and Formanek H 2005 3D analysis of chromosome architecture: advantages and limitations with SEM *Cytogenetic Genome Res.* **109** 70–8
- Waterman P C 1965 Matrix formulation of electromagnetic scattering *Proc. IEEE* **53** 805–12
- Wax A, Yang C, Backman V, Badizadegan K, Boone C W, Dasari R R and Feld M S 2002 Cellular organization and substructure measured using angle-resolved low-coherence interferometry *Biophys. J.* **82** 2256–64
- Yurkin M A and Hoekstra A G 2011 The discrete-dipole-approximation code ADDA: capabilities and known limitations *J. Quant. Spectrosc. Radiat. Transfer* **112** 2234–47
- Yurkin M A, Hoekstra A G, Brock R S and Lu J Q 2007 Systematic comparison of the discrete dipole approximation and the finite difference time domain method for large dielectric scatterers *Opt. Express* **15** 17902–11